Mechanisms Leading to Stabilization and Incomplete Combustion in Lean CH4/H2 Swirling Wall-Impinging Flames

Luming Fan, Bruno Savard, Benoît Fond, Antoine Durocher, Jeffrey Bergthorson, Spencer Carlyle, Patrizio Vena

Mechanisms leading to stabilization and incomplete combustion in lean CH_4/H_2 swirling wall-impinging flames

Luming Fan[a], Bruno Savard[b], Benoît Fond[c], Antoine Durocher[a,d], Jeffrey Bergthorson[d], Spencer Carlyle[a], Patrizio Vena[a,*]

[a] *Aerospace Research Centre, National Research Council, 1200 Montreal Road, Ottawa, ON K1A 0R6, Canada*
[b] *Department of Mechanical Engineering, Polytechnique Montréal, Montréal, QC H3T 1J4, Canada*
[c] *ONERA - The French Aerospace Lab, 8 rue des Vertugadins, 92190 Meudon, France*
[d] *Department of Mechanical Engineering, McGill University, 845 Sherbrooke Street West, Montréal, QC H3A 0G4, Canada*

Abstract

In gas turbines, confined highly turbulent flames unavoidably propagate in the vicinity of a relatively cool combustor liner, affecting both the local flame structure and global operation of the combustion system. In our recent work, we demonstrated, using simultaneous [OH] × [CH_2O] PLIF and stereo-PIV, that lean CH_4/H_2 flames at a high Karlovitz number can present a highly broken structure near wall, highlighted by a diffuse CH_2O cloud which suggests local quenching and incomplete oxidation. Such high Karlovitz numbers were achieved using an inclined plate, which substantially extended the lean flammability of the low swirl flames. Yet, how a cooled wall acting as a heat sink played a conducive role in stabilizing high Ka flames remains unanswered. In addition, the origin of the CH_2O cloud is also unclear. Hence, in this work, we look to better understand the stabilization mechanisms for lean and ultra-lean flames on the same configuration, and how they may change with a parametric variation of plate incident angle, plate-nozzle distance, and bulk velocity up to the critical values that lead to flame blow off. The results show that the impinging swirling flow creates a low speed region that helps hold the flame, while the wall prevents mixing with ambient cold air. The

*Correspondence: patrizio.vena@nrc-cnrc.gc.ca

Preprint submitted to ASME Turbo Expo 2023

production of diffuse CH_2O, which indicates the occurrence of local quenching, is associated with a mean strain rate K beyond the extinction strain rate K_e. For CH_4 flames, most of the reaction zones reside within $|K|/K_e < 1$; for 70% H_2 flames at $\phi = 0.4$, the reaction zones are highly broken and scattered in a large area where $|K|/K_e < 8$, the interspace of which is fully filled by CH_2O. In other words, high H_2 fraction flames appear to be more robust to persistent strain rate, thus extending their stability envelope. However, these flames can subsist as highly broken flames featuring strong incomplete combustion.

Keywords: Lean combustion; flame stabilization; hydrogen; heat release rate; mean strain rate

---

1. Introduction

Lean combustion of low to zero-carbon fuels is among the primary goals for the energy and aviation sectors for the coming decades [1]. Hydrogen, in particular, has the potential to both lower our dependence on traditional fossil fuels while also greatly reducing, even eliminating, emissions of CO and CO_2. Hydrogen/air mixtures are further capable of stable operation under ultra-lean conditions with lower flame temperature, such that they may also lead to reduced emissions of NO_x. However, this can lead to unwanted thermoacoustic instabilities resulting in damaged engine components [2, 3] and potential safety risks, while also causing local quenching of the flame where it is too lean or near a solid boundary (flame-wall interaction, FWI) and subjected to substantial heat loss. In combustion research, high Karlovitz number (Ka) flames are highly relevant to the lean burning conditions, where Ka is defined by the ratio of the chemical time scale of the reactions over the turbulence Kolmogorov time scale [4]. A high Ka flame is typically characterised by a lean fuel mixture burning in highly turbulent flows. Studies on high Ka flames, especially those flames in the thin reaction zones ($1< Ka<100$) and broken reaction zones ($Ka>100$) regimes are gaining increasing attentions recently, e.g. [5, 6].

In a number of FWI studies, it has been demonstrated both experimentally and numerically that the flame — even near stoichiometry where the flame speed is relatively high, and subjected to a laminar or moderate turbulent flow condition, i.e., a low Karlovitz number — will be quenched near the wall and produce a considerable amount of pollutants such as CO [7, 8]

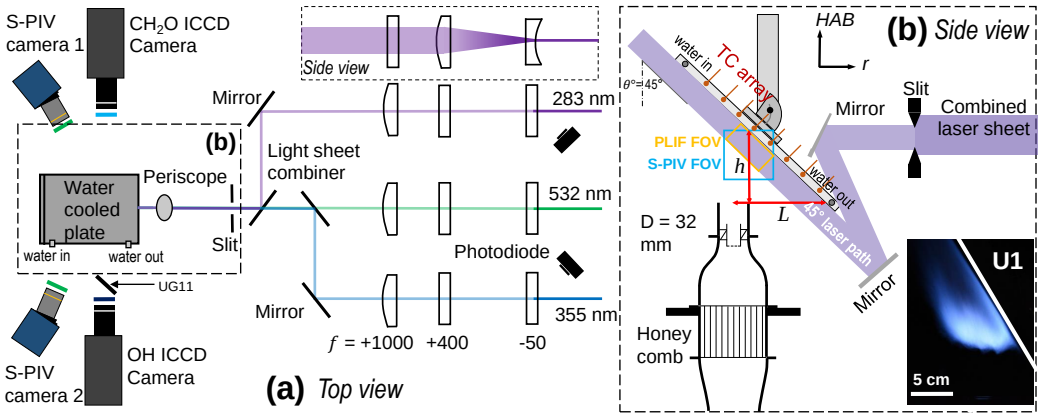

Figure 1: (a) Top and (b) side view of the experimental setup

due to a low reaction temperature. These observations inevitably bring in concerns that for the lean and ultra-lean combustion targeted by industry, the reactions would be much less robust in the vicinity of the cooled combustor liners, producing even more incompletely oxidized intermediates, and experiencing extensive local quenching that might further progress to blow off of the entire flame. Hence, FWI at a high Karlovitz number is an urgent topic that calls for more investigations. To date, however, most of the previous FWI studies, especially for side-wall quenching, have focused on mildly lean or near stoichiometric conditions, where Ka is relatively low. Previous work on FWI has also investigated the fuel effects on quenching distance and emission, using, e.g. CH_4 and DME [9], biogas/H_2 [10], and recently ammonia [11]. The behaviors of high H_2 fraction or even pure H_2 flames in FWI must therefore be further explored.

For such a purpose, we previously investigated FWI at high Ka using simultaneous [OH] × [CH_2O] PLIF and stereo-PIV [12]. In that study, lean and ultra-lean CH_4, CH_4/H_2, and H_2 flames were ignited on a low-swirl burner (LSB) that resembles model gas-turbine combustors [13] with an inclined side wall cooled by water. That configuration deviates from previous FWI studies that are categorized by idealised head-on quenching (HOQ) and side-wall quenching (SWQ), as it provides a flame-wall interaction scenario in which flame impinging that causes both high strain in the flow and substantial heat loss to a relatively cool wall co-exist, similar to that occurring in gas-turbine combustors. Another reason for using this inclined setup is to ensure a high PLIF image quality by shining the laser sheets from the

cold fresh gas side and parallel to the wall, hence minimizing beam steering effects due to changes in the refractive index in the high temperature products as well as suppressing near wall reflections. Using this configuration, we observed unique flame structures at high Ka ranging from around 30 (thin reaction zones regime). A highly broken flame front was found near the wall with increasing H_2 fraction, and diffused formaldehyde (CH_2O) pockets were identified in the same area, suggesting that in the near wall region, the flame may have entered the broken reaction zones regime due to high turbulence and heat flux to the wall. When we further reduced the equivalence ratio (Ka increased to up to 1100, in broken reaction zones regime), close to blowoff, the entire flame became highly broken with an extensive diffuse cloud of CH_2O formed downstream, indicating severe incomplete oxidation of hydrocarbons. This brings a new concern that with certain geometries a combustor may stabilize H_2/hydrocarbon fuel blends at an extremely low equivalence ratio, at which the hydrocarbon fuel is only partially oxidized and yet the flame is sustained.

Intriguingly, the inclined side wall in our previous work provided such a suitable flow condition that greatly extended the lean flammability limit. Compared to the no-wall configuration, gas mixtures could be ignited for equivalence ratios that were 0.04-0.18 leaner as the H_2 fraction increases. A 70% H_2 flame at a minimum laminar flame speed at 2.06 cm/s ($\phi = 0.37$), was successfully sustained. For 100% hydrogen flames, ϕ can be as low as 0.22. On the contrary, the minimum achievable equivalence ratio for the same 100% hydrogen flames without the inclined wall was 0.4. In the same paper, we also compared flame behaviour with both a water cooled and a relatively hot adiabatic ceramic wall, and did not observe a change in lean flammability, indicating that the thermal boundary condition does not play an important role for such ultra lean flames, as they stabilize far away from the wall and their stabilization is dominated by the flow field rather than the heat loss to the wall. In this paper, we look to build on our previous findings and investigate the flow dynamics that lead to this extended stability range by varying the plate angle, plate-nozzle distance, and bulk flow velocity.

2. Experimental setup and data processing

Figure 1 shows the experimental apparatus previously described in [12]. Briefly, two UV lasers at 282.94 nm and 355 nm were used to excite OH and CH_2O, respectively. The 355 nm laser pulse is delayed by 400 ns relative to

the 282.94 nm in order to avoid interference between the two channels. A 532 nm double-pulse PIV laser was run simultaneously to perform stereo-PIV. Both UV pulses were fired in the middle of the two 532 nm pulses, such that the flame moved negligibly during the 400 ns delay so the flame structure revealed by the fluorescence signals matched well on the two channels. The laser beams were first expanded by similar cylindrical lens combinations, each coated for the corresponding wavelength, to form three separate collimated light sheets. The three light sheets were then combined with two dichroic mirrors (beam combiners). A periscope consisting of two aluminum coated broadband mirrors (Zerodur®, Thorlabs PF2011) with a high damage threshold was carefully aligned to re-direct the combined light sheets from beneath the plate so that they were parallel to the inclined surface (see Figure 1), avoiding strong laser flare caused by directly shining the laser sheets on the solid boundary. Two ICCD cameras (PIMAX2) equipped with a UV lens were configured on the opposite sides of the burner to capture the OH and CH_2O PLIF images. A 320 $\pm$ 20 nm bandpass filter for OH, and the combination of a 395 nm longpass and a 500 nm shortpass filter for CH_2O, were installed in front of the corresponding cameras to suppress background noise and flame luminosity. A color glass filter (Schott UG11) transmitting OH signal while absorbing/reflecting CH_2O signal was placed at 45° in front of the OH camera to avoid direct reflection of CH_2O signal into the opposite camera, see Figure 1. Due to the slow readout speed of the PIMAX2 ICCD cameras, the entire system was running at 2 Hz. The ICCD cameras were installed on adjustable angle platforms (Thorlabs AP180) and tilted by an angle such that the PLIF field of view is always made parallel to the plate, as marked by the orange rectangle in Figure 1. In such a way, the number of readout pixel columns is minimized to allow a maximum 2 Hz frame rate for a 30.8 $\times$ 79.9 mm^2 (350 $\times$ 900 pixels at a projection resolution of 87.9 μm/pixel) field of view (FOV). For each dataset, 500 images are collected to converge the statistics.

In order to observe the entire flame structure, for all test cases, we conducted separate OH PLIF measurements with a horizontal laser sheet and PLIF camera views, by replacing the periscope by three mirrors, re-directing the lasers to incident from the left side in Figure 1(b) and shine on the plate surface horizontally. The position of the focusing lens used to narrow down the 282.94 nm light sheet was adjusted accordingly so that the light sheet remains focused over the test section. CH_2O PLIF with a horizontal 355 nm light sheet is not possible as the CH_2O signal will be entirely submerged into

the strong background noise from the spark produced by the intense laser heating on the black surface.

Two sCMOS cameras (LaVision Imager sCMOS) were operating in double frame mode to capture the two 532 nm pulses. The pixel resolution was 31.9 μm, measured by a target from La Vision. PIV processing was conducted in Davis 8.4, using a 32 $\times$ 32 pixel interrogation window and 50% overlap. The final vector inter-spacing was 0.47 mm. The scalar fields including in-plane vorticity ω and mean strain rate K were also extracted from the calculated vector field in Davis. The OH and CH_2O PLIF images were accurately mapped and spatially registered using a specialized target. The mapping error is less than 1 pixel. The PLIF images were then corrected for pulse-to-pulse laser energy fluctuations (recorded by two Photodiodes) and laser profile. The 282.94 nm laser profile was obtained using the fluorescence signal from a uniform acetone vapor field, whereas 355 nm laser profile was measured directly from Rayleigh scattering. The product of corrected OH and CH_2O image then yields the heat release rate (HRR) distribution, as [OH] $\times$ [CH_2O] has been proven to be a good heat release marker for CH_4 [14] and CH_4/H_2 flames [12].

A well-characterised low-swirl burner (LSB) [13] was used in the present study. LSBs are a generic burner developed for gas turbine combustors [15], which were later widely used to characterise flame structures and dynamics, e.g. in [16]. The nozzle diameter at the burner exit is 32 mm, and the swirl number is estimated as 0.47. A 40 $\times$ 60 cm^2 water-cooled stainless steel plate was fixed on the right side and inclining towards the burner, stabilizing the flame at lean and ultra-lean conditions that otherwise cannot be ignited. The plate inclination angle can be adjusted from 0° (i.e., a vertical wall like those used in previous SWQ studies [9]) to 90° (a horizontal impinging wall in HOQ studies [17]). In the present study, two plate angles, 30° and 45°, are investigated for their roles in flame stabilization. The laser path was changed according to the plate angle by adjusting the two mirrors in the periscope to ensure the light sheets remained aligned with the plate. The burner was installed on a 3-axis traverse so that the flame position can be shifted along the plate relative to the camera FOV while keeping the nozzle-plate distance constant. The surface temperature of the plate was derived from the temperature gradient measured by thermocouple (TC) arrays embedded at different depths and axial locations. An IR thermal camera was also used to image the surface temperature immediately after the flame was turned off. Both methods showed a uniform surface temperature

distribution around 330 ± 8 K in the center of a 30 × 40 cm^2 region of interest, which fully covers the flame-wall interaction zone. Beyond this area, the surface temperature gradually drops to 296 K at the edges away from the reaction zone. A 1 mm thin stainless steel wire was mounted to the surface of the plate roughly 15 cm downstream of the flame cone, so that condensed water formed on the upper half of the cooled-surface did not drip back to the reaction zone, but instead led to one side of the plate, where the water was collected in a beaker. Since the thin wire is far downstream of FWI region of interest, it is expected to have negligible influence on the flow field and the reactions upstream. The entire plate surface was spray-painted black to suppress laser reflection and other undesired noises, while the thin paint layer (< 10 μm) does not alter the thermal property of the plate surface.

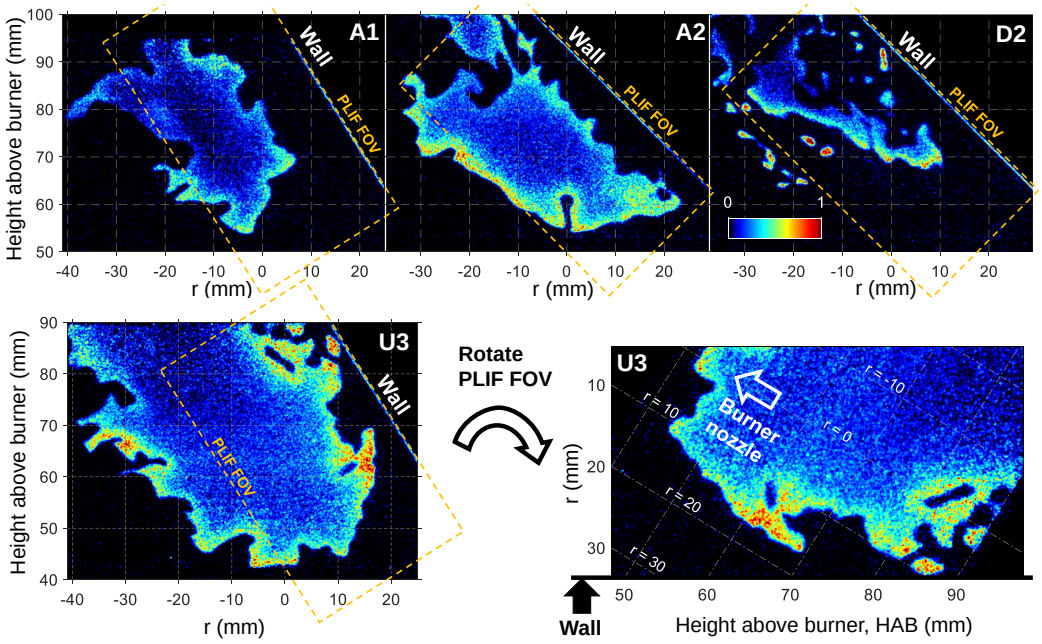

Figure 2: Example OH images taken with a horizontal 283 nm light sheet, revealing the entire impinging flame structure. The dashed rectangle roughly illustrates the FOV of the tilted PLIF ICCD cameras. An example image adjusted for the incident plate angle θ, i.e. rotated by $90° + \theta$, is provided in the second row.

Table 1: A summary of test conditions

Case	θ (°)	L/D(-)	h/D(-)	U (m/s)	ϕ (-)	CH_4:H_2*	P (kW)
A1	[**30**°]**	2	2.6	10	0.68	100:0	16.9
A2	45°	3	2.5	10	0.68	100:0	16.9
D1	45°	[**2**]	1.5	10	0.40	30:70	10.5
D2	45°	3	2.5	10	0.40	30:70	10.5
D3	45°	[**4**]	3.5	10	0.40	30:70	10.5
U1	30°	2	2.6	[**6**]	0.78	100:0	11.5
U2	30°	2	2.6	8	0.78	100:0	15.3
U3	30°	2	2.6	10	0.78	100:0	19.1
NW	–	–	–	10	[**0.78**]	100:0	19.1

* The fuel ratio is defined by mole (volume) following the same approach outlined in [13]. ** The values in bold font inside the brackets are close to extremities for that flame to blow off.

3. Operation conditions

In the present study we investigate the effects of (1) plate angle θ, (2) plate-nozzle distance L/D, and (3) bulk velocity U at the burner exit on flame stabilization for different CH_4/H_2 flames. The test conditions are summarized in Table 1. The reactants were fully premixed before entering the burner for all test cases.

In our previous work [12], we tested 100% CH_4, CH_4/H_2, and H_2 flames at lean and ultra-lean conditions for the same inclined wall at 30°, and achieved very high Karlovitz numbers (Ka) ranging from 26-1100. For flames close to blow off, the flammability range is usually very narrow and highly susceptible to any changing parameters, especially for pure methane flames without H_2 addition. Here, we slightly increase the equivalence ratio to extend the applicable range of the parameters of interest, and thus allow systematic observations on the flame behavior caused by those changes. We use 100% CH_4 flames at $\phi = 0.68$ and 0.78 for investigations of the plate angle (A cases in Table 1) and the bulk velocity at the burner exit (U cases) respectively, and a 70/30% (by volume) H_2/CH_4 flame at $\phi = 0.4$ for plate-nozzle distance (D cases). The laminar flame speed S_L^0 for the three flames are 18.1, 26.0 and 3.9 cm/s. The laminar flame speed and thickness S_L^0, and the mean extinction strain rate (ESR) K_e mentioned later on, were all calculated with Cantera using GRI-Mech 3.0 [18]. It must be noted that at the thermochemical con-

ditions and bulk velocity considered, the flame can survive without the wall only for case U3. The total flame power P (kW) of each case is also listed in Table 1.

For A cases, the plate angle is varied from 30° to 45°, with the former near the blow-off limit at these thermochemical conditions (the flame cannot survive at lower angles). The nozzle-plate distance L/D also changed from $2D$ to $3D$ to keep a similar h/D for these two cases, where h is the vertical distance from the right edge of the burner nozzle to the plate surface, as illustrated in Figure 1. h/D roughly defines the height of the impinging point for the lean flames and thus the position where flame-wall interaction starts.

For D cases, the minimum and maximum plate-nozzle distances to stabilize the flame are $2D$ (Case D1) and $4D$ (Case D3) for $\theta = 45°$, and $1.5D$ to $3D$ for $\theta = 30°$ (not shown in this paper).

For U cases, the velocity range is 6-15 m/s, with the plate at 30° and $L/D = 2$. Since the A and D cases are all close to the maximum applicable velocity for the corresponding configuration, here in U cases, we chose 10, 8, 6 m/s in order to approach an 'internal blow-off region' observed in our previous work [13]. We also conducted a reference case with no wall, Case NW, for a 100% CH_4 flame. For case NW, both the periscope and the plate were removed to recover the setup in [13].

4. Flame structure and flow field

4.1. Flame structure

Figure 2 shows sample OH images recorded with the horizontal light sheet for Cases A1, A2, D2, and U3, revealing the entire flame structure. A thin luminescent line on the right side of the flame cone, possibly the emission from the black paint, marks the wall position. Consistent with our previous observation, in A1 and A2, the 100% CH_4 cases, the flame brush stays far from the wall, but the distance will gradually reduce as the mixture goes richer, see U3; whereas for D cases with 70% H_2, the highly broken OH structures are observed on both sides of the flame cone, which penetrate into the swirling flow region. Although the laminar flame speed is lower for the D cases, flame speed has been observed to increase significantly more in the presence of turbulence for H_2 flames, compared to CH_4 flames [19]. Previous numerical studies [20, 19] also reported that at a high Ka, broken flame structures are formed in H_2 flames due to thermal-diffusive instability, which

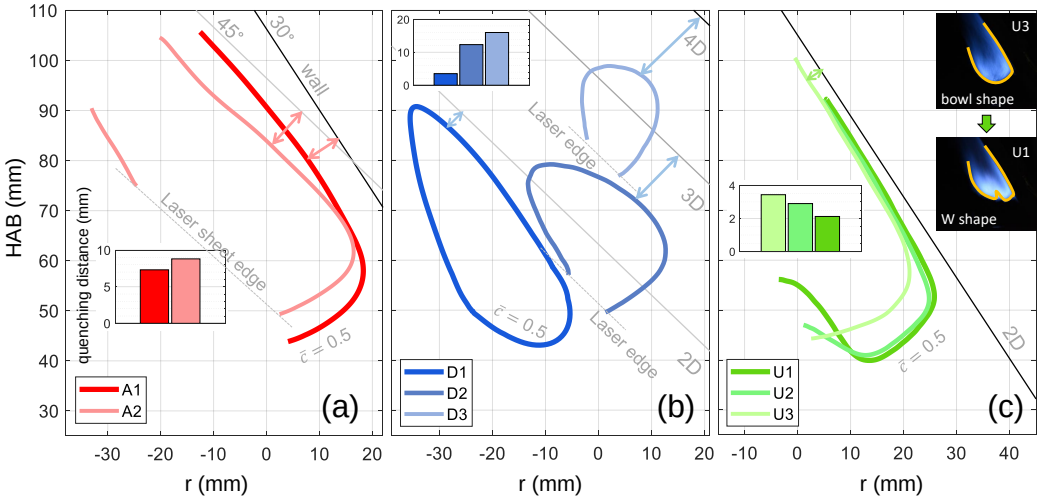

Figure 3: Flame brush position marked by the mean progress variable iso-contours $\bar{c} = 0.5$ for A, D, and U cases. The minimum distance from the iso-contour to the wall is shown in the bar plots for each case.

are transported to a wider area by strong turbulence, similar to the structure observed in case D2 in Figure 2. On the contrary, a continuous flame front is formed in the central jet region, where both the velocity and turbulence intensity are relatively low. In Figure 2, we marked the PLIF FOV of the tilted ICCD cameras by the dashed rectangle. To save space throughout the paper, PLIF images in Figures 6, 7, 8, and 9 are adjusted for the incident plate angle θ, such that the wall lies horizontally at the bottom edge of each image. An example is provided in the second row Figure 2.

Figure 3 plots mean progress variable $\bar{c} = 0.5$ iso-contours for all cases A, D, and U for corresponding wall incident angles 30/45 degrees and positions $2D/3D/4D$. The sub-figures show bar plots of the minimum distance from the $\bar{c} = 0.5$ iso-contour to the wall, here defined as the mean quenching distance. As shown in Figure 3(a), increasing the plate angle further pushes the flame downstream and towards the unconfined side of the flow. However, the quenching distance remains nearly the same. For D cases shown in Figure 3(b), substantial differences appear when moving the plate away from the burner for $2D$, $3D$, and $4D$. At $2D$, the flame cone is elongated substantially along the wall and pushed to the left side of the burner center line. The flame cone is lifted accordingly as L/D increases while the kernel size is shrinking, indicating a weaker flame close to blow off. The quenching distance increases

from 3.5 mm in D1 to 16 mm in D3, likely due to a higher extent of mixing with the ambient cold air at such a high height above burner (HAB) of 90 mm, leading to a weaker mixture strength with lower equivalence ratio near the wall than at the burner exit. Figure 3(c) shows the flame position for U cases. As the bulk velocity reduces from 10 to 8 m/s, the leading edge of the flame moves upstream along the plate by about 7 mm. However, when further decreasing the velocity from 8 to 6 m/s, the leading edge position does not change much. Instead, the flame shape starts to change from a bowl shape to a 'W' shape, as shown by the flame pictures in the sub-figure. The same trend was observed without the plate for 100% CH_4 at $\phi = 0.8$ in [13]. For the NW case, the minimum flow velocity to stabilize the flame is 10 m/s. Below this value, the gas mixture drops into the internal blow-off regime as mentioned earlier, until the bulk velocity further drops to 4 m/s, where the mixture can be ignited again and the flame presents a 'W' shape. Interestingly, with the presence of the inclined plate, this internal blow-off regime is significantly reduced. The velocity gap where the mixture cannot be ignited only ranges from 4-6 m/s, much narrower than the 4-10 m/s range for the NW case.

For lean and ultra lean cases, as indicated by the progress variable iso-contours, the flame brush remains quite far from the wall ($>$ 10 mm in cases A, and D2, D3). In our previous paper [12], we reported that under such conditions, the flame structure barely changes between the cooled and ceramic plates (which provides a nearly adiabatic thermal boundary condition), nor did the ceramic wall help further stabilize the flame at leaner conditions. In that study, we found that the progress variable iso-contours, which mark the flame brush position, for the ultra lean flames with the isothermal and the adiabatic wall were perfectly overlapped[1], again suggesting that the flow field is here the dominating factor in flame stabilization rather than heat loss to the wall. For case D1 (minimum plate-to-nozzle distance for that flame to survive), heat loss to the wall may be an equally important factor as the flow dynamics, as the flame front is pushed sufficiently close to the cold wall. Similarly for the U cases, as the bulk flow rate reduces, the proportion of heat loss to the total heat produced by the flame increases, increasingly contributing to flame blow-off.

[1]The progress variable iso-contours for both thermal boundary conditions can be found in supplementary material 4 in [12].

4.2. Velocity field

Figure 4 shows the mean velocity field of cases U3 and NW (both 100% CH_4, $\phi = 0.78$) measured by a highly diverging 532 nm light sheet incident from beneath the plate. The mean progress variable iso-contours extracted from the ensemble average of individual binarized OH images are superimposed on the velocity field to illustrate the flame shape and position relative to the flow field. The background color represents the magnitude of the three-component velocity. Comparing with the near symmetric NW flame shape shown in Figure 4(b), the flame brush on the confined side is strongly altered by the wall and sharply redirects the flame. At the same equivalence ratio $\phi = 0.78$, the flame leading edge in U3 located at a lower height (HAB = 45 mm based on $\bar{c} = 0.5$) than the NW case (HAB = 50 mm). This is similar to a head-on impinging flame where a bluff-body helps anchor the flame by altering the flow field.

We compare the mean and rms velocity profiles extracted from the same height in U3 and NW, and present the results in Figure 5. Between 50 mm and 60 mm, the flame brush touches the wall and bends, causing the right peak of the velocity profile in U3 to drop significantly, as highlighted in Figure 5 with the yellow arrows. The impingement slows down the swirling flow on the confined side. We examined all the lean and ultra-lean conditions, and found that the flame front always anchored at similar HAB where it is impinged by the wall (see Figures 6 and 7 in the present paper and also the figures in our previous work [12]). This strongly suggests that the survival of the flames is associated with the presence of a low-velocity region caused by the impinging wall, similar to the stabilization of head-on impinging flames. The turning flow also increases the residence time of the hot products[2], and brings heat back to the central non-swirling flow, instead of dispersing it into the ambient air. This is evidenced by the fact that if the plate angle is too small (e.g. a vertical wall), or the plate is too far away, no 100% CH_4 cases can be ignited below $\phi = 0.78$ as the flow velocity is not sufficiently reduced. The low velocity region further explains the trend in the quenching distances shown in Figure 3(c). For case U3 (10 m/s), the quenching distance is much smaller (3.7 mm) as the higher flame speed (26 cm/s) enables the flame to stay in a higher velocity region compared to A1 (8.3 mm, 18.1 cm/s). As the

[2]Similar to the role of recirculation in some MILD combustors [21] designed to burn intense CO_2 diluted biogas fuels.

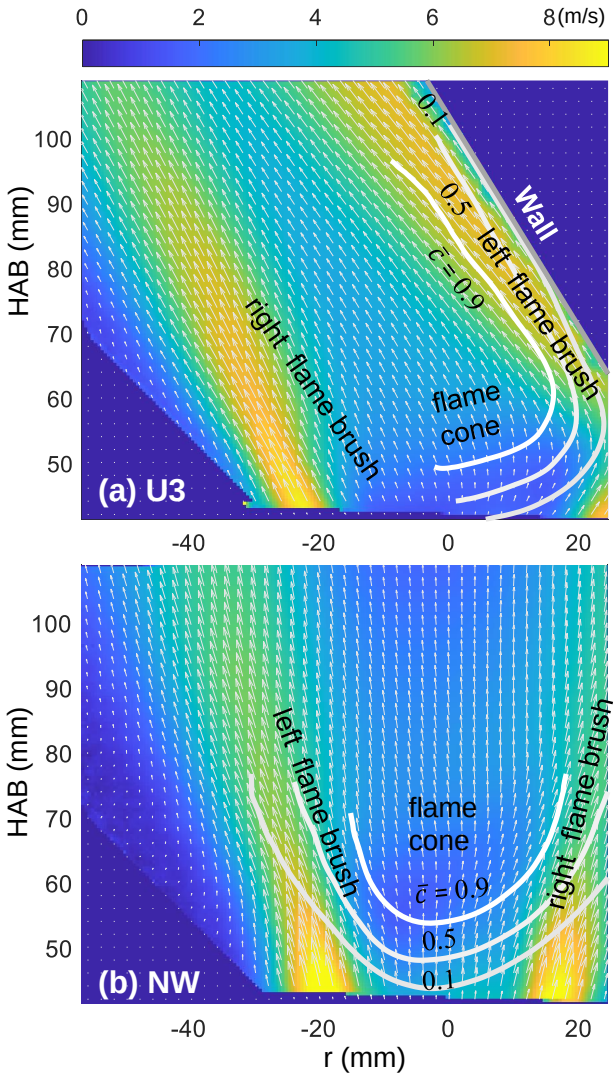

Figure 4: Mean velocity field of (a) U3 and (b) NW. Mean progress variable iso-contours $\bar{c} = 0.1$, 0.5, and 0.9 are superimposed on the velocity field. The background colors show the magnitude of the three-component velocity. The vector density is reduced by a factor of 0.25 for better display.

bulk velocity gradually decreases from 10 to 6 m/s, the mean velocities near $\bar{c} = 0.5$ iso-contour are 6.9, 3.9 and 2.5 m/s (for U1, U2, and U3 respectively) at the height where the minimum distance to the wall is found. Subsequently, the quenching distance for the three cases gradually decreases from 3.4, 2.9,

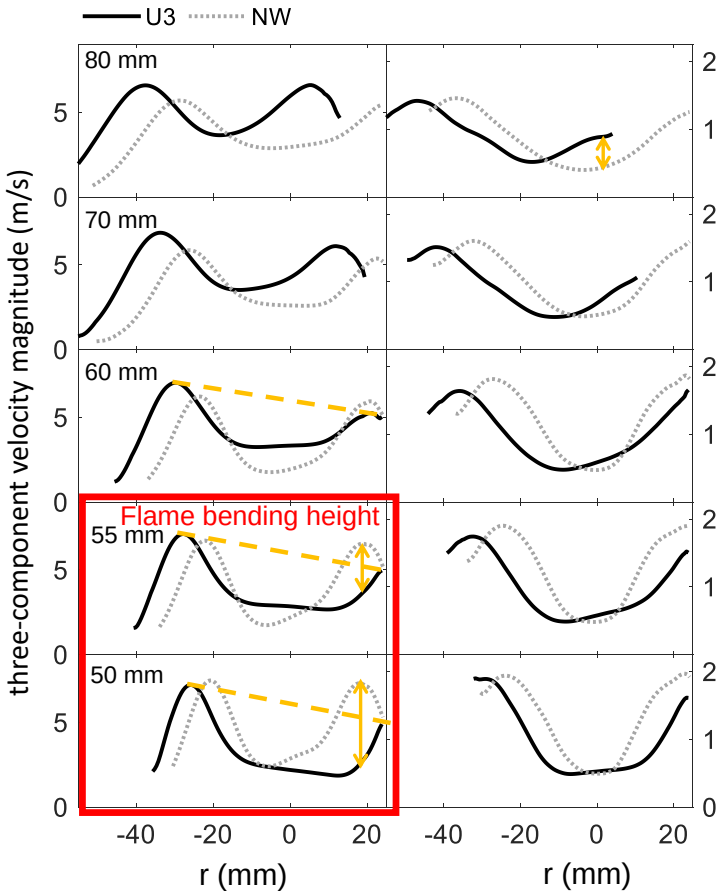

Figure 5: Comparison of mean and rms velocity profiles extracted from Figure 4 at the same heights in U3 and NW.

and 2.1 mm. Downstream of the flame front (HAB > 60 mm), the flow is accelerated along the wall due to thermal expansion. The entire velocity profile (Figure 5) is pushed towards the negative radial position relative to its counterpart (gray dashed line) at all heights.

The rms velocity profiles show a broader low rms region in U3 than the NW case below HAB = 70 mm. This is caused by a combined effect of the shifted profile towards the negative radial positions, and the fact that the impingement also dampens the velocity fluctuations while reducing the flow velocity on the confined side. HAB > 70 mm, the rms velocity in the near wall region goes about 50% higher than that in the NW case, as the turbulent vane flow is pushed back towards the burner center.

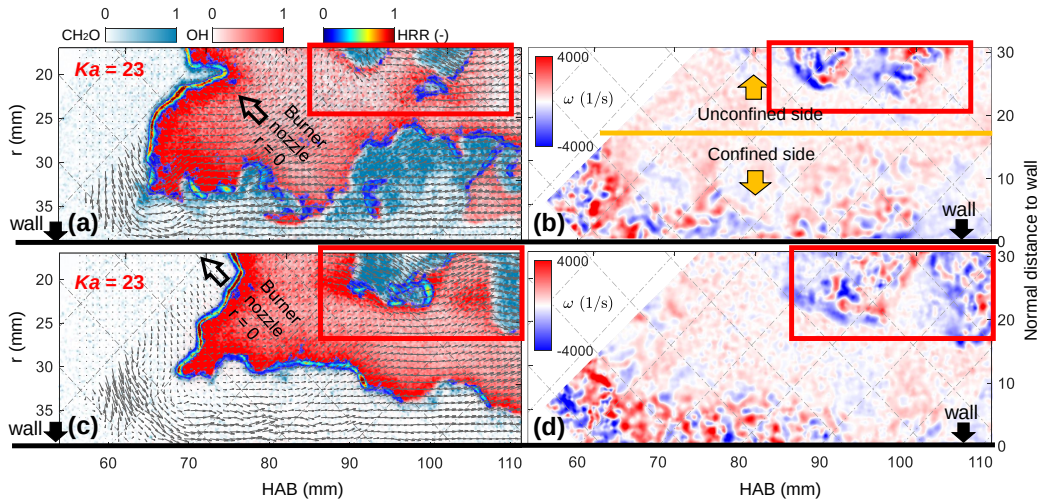

Figure 6: Left column: Two single shots OH (red), CH_2O (green-blue), and heat release rate (jet) of case A2, superimposed by the simultaneous velocity field; The hollow arrows are pointing towards the burner nozzle lying outside the FOV. Right column: the corresponding vorticity field calculated from the instantaneous velocity field. Such rotated FOV was illustrated in the global coordinated shown in Figure 2. The diffusive CH_2O signal is always associated with a higher local vorticity, as highlighted by the red rectangle. Case A1 shows the same correlation on the unconfined side, though CH_2O appears much less frequently due to the imaging field of view.

5. Flame quenching and formaldehyde cloud

Figure 6 (a)(c) shows two example single shot PLIF images of A2. The images are corrected for the incident plate angle θ as explained in Figure 2, where ticks on the left and bottom axes represent the radial position and HAB, respectively. The Cartesian coordinates defined by r and HAB are at the angle θ with the plate, as illustrated by the gray dot-dashed lines. The burner nozzle is located in the top-left direction outside the image. The red colormap represents normalized OH signals, while the green-blue shows CH_2O. Their product, or the HRR, is superimposed on the PLIF signals by a jet colormap. The HRR image is self-normalized by its 99.7% value (and not its maximum due to potential erroneous hot pixels in an image). Simultaneous velocity fields obtained by stereo-PIV are also converted to fit the PLIF FOV. The vector density of the instantaneous velocity field is reduced by a factor of 0.4 for clearer display.

The two single shots in Figure 6 present a typical lean CH_4 flame struc-

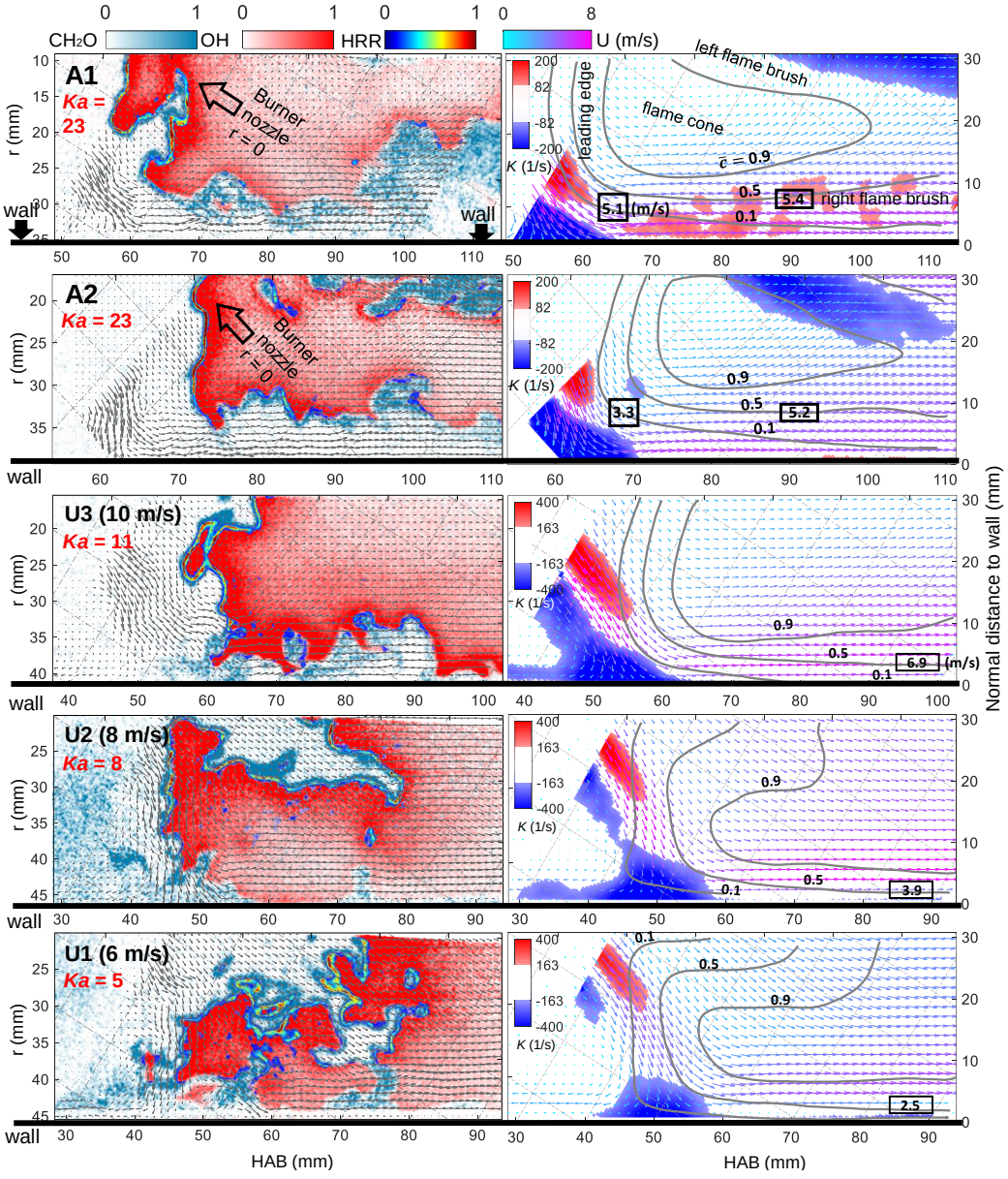

Figure 7: Left column: Example single-shot OH (red), CH_2O (green-blue), heat release rate (jet), and the simultaneous velocity field for A and U cases. Right column: The mean strain rate (blue-red heat map), superimposed by the mean velocity field (vector arrows with color) and the mean progress variable iso-contours. Areas where the mean strain rate lower than the mean extinction strain rate (ESR) is marked white.

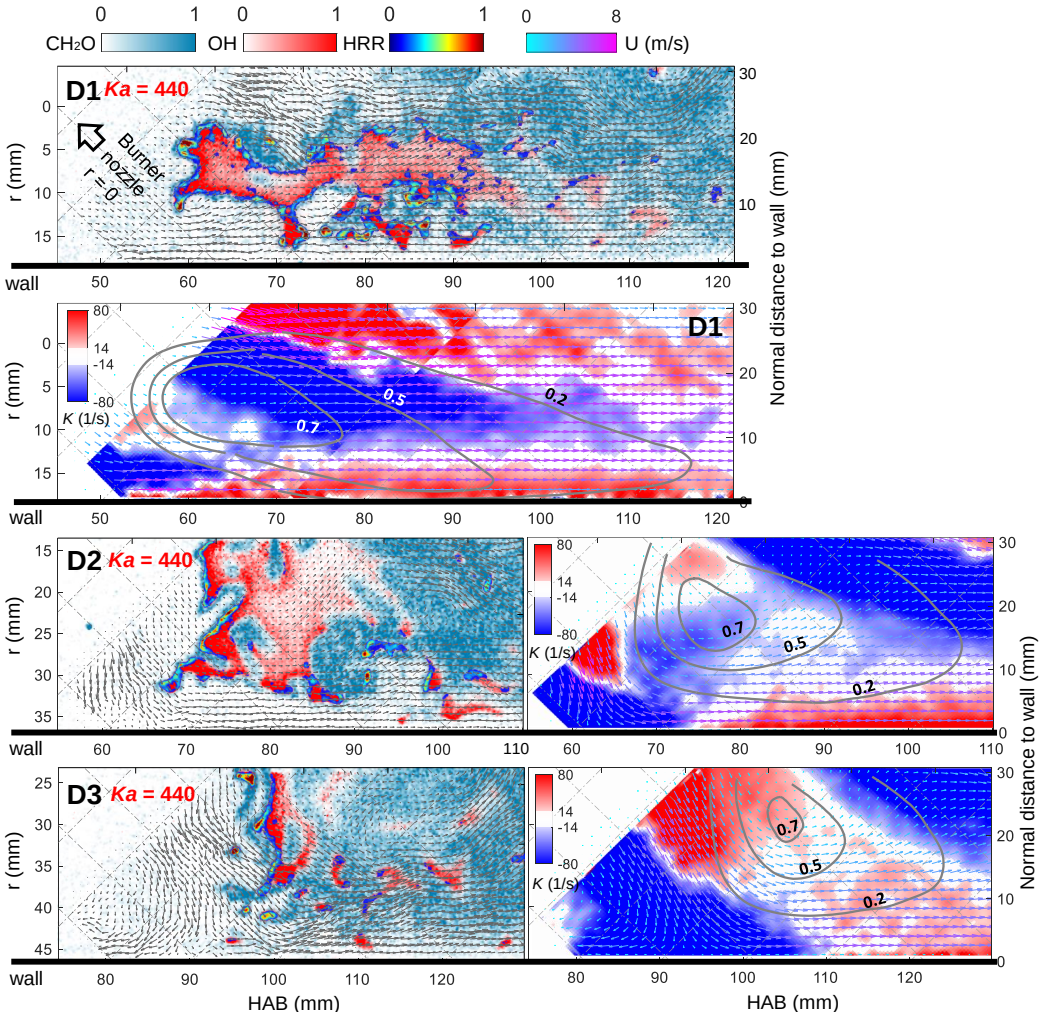

Figure 8: Example single-shot results for D1-D3, and the corresponding mean strain rate field. Areas where the mean strain rate is lower than the extinction strain rate (ESR) are marked white. Images of D1 were reconstructed from two measurements taken at different HAB in order to show the elongated flow field.

ture in the present FWI configuration: a thin layer of CH_2O is formed just ahead of the flame leading edge, followed by a robust OH signal. Strong and continuous HRR distribution is also identified here. In contrast, diffuse CH_2O is identified on both sides of the flame cone. The CH_2O pockets found on the free mixing side are associated with strong local vorticity, as shown by Figure 6(b)(d). The fact that the flame is in the shear layer and that less

viscous dissipation occurs at low temperature may explain the higher vorticity found on the reactants side. The thick formaldehyde layer is formed likely due to mixing with air that causes a lower equivalence ratio and a larger flame thickness, probably also combined with a local mean strain rate beyond the extinction strain rate K_e (see Figure 7).

We present example single shot images for A1-U3 in the left column of Figure 7. In the right column, the mean strain rate is plotted in a blue-red colormap, together with the mean velocity vectors (vector density reduced by a factor of 0.3) whose color represents the three-component velocity magnitude, and the $\bar{c}$ iso-contours extracted at 0.1, 0.5, and 0.9. For D cases, $\bar{c}$ = 0.9 is either too small or does not exist, whereas the $\bar{c} = 0.1$ is too close to the wall in case D1; Hence, we choose 0.2, 0.5, and 0.7 instead to show the flame position for D cases. To illustrate the role of mean strain rate, areas where the mean strain rate is lower than the extinction strain rate (ESR) are marked white.

The first two rows in Figure 7 show cases A1 θ=30° and A2 θ=45°. Unlike the free-mixing side, most of the formaldehyde, though still more diffuse than those produced at the flame leading edge, is distributed within only a few millimeters from the OH signal, especially in A2. In our previous work [12], we hypothesised that the high persistent strain rate exceeds the mean extinction strain rate (ESR) of the flame and causes local quenching in the near wall region, where intermediate products from incomplete combustion such as CH_2O are produced locally and cannot be further oxidized. High CO concentration may also be detected in the same region if CO-LIF is performed as done in [8, 7]. Compared with A2, A1 has a slightly thicker CH_2O brush near the wall. In fact, in many instantaneous single shots of A2, e.g. in Figure 6(c), the flame front against the wall is as robust as the flame leading edge, also suggesting a lower mean strain rate may assist full oxidation of the intermediates at lean conditions. If we further compare A1 with case S1 in [12], where all the conditions are the same except that S1 is leaner, at $\phi = 0.65$, $S_L^0 = 15.4$ cm/s and ESR = 64 s^{-1}, the CH_2O signal filled the entire gap between the flame cone and the wall, as more extensive local quenching took place owing to an even lower ESR for the leaner gas mixture. Note that even though the mean strain rate near the wall in A2 is lower than A1, the progress variable contour $\bar{c}$ did not move closer to the wall, as the near wall velocity for the two cases are equally high (5.4 and 5.2 m/s).

The last three rows in Figure 7 show the U cases. Compared to cases A,

most of the flame fronts in cases U are robust, characterised by a thin and focused CH_2O layer. As the bulk velocity is decreased from U3 to U1, the large gap between the flame cone and the wall disappears, as velocity near the wall becomes sufficiently small compared to the local turbulent flame speed. The quenching distances are now only of several times the flame thickness (0.55 mm for U cases), falling back to conventional definition of previous FWI studies, as summarized in [22] for a variety of fuels. Another trend observed for U3-U1 is that the flame front on the unconfined side becomes increasingly twisted, as the flame front is freely propagating towards low speed regions inside the central jet. We plot the CH_2O probability map by ensemble averaging binarized CH_2O, and present the results of A1, U1, and D1 in Figure 9, which are all close-to-blow-off cases. Figure 9 shows that the recirculation zone formed by the wall extracts significant amount of CH_2O out from the reaction zone in case U1. This could contribute, in addition to heat loss to the wall, to extinguish the flame upon further reducing the bulk velocity.

D cases show the 70% H_2 burning at an ultra-lean condition $\phi = 0.4$. The most characteristic trait of ultra-lean flames is the large CH_2O cloud formed downstream of a small flame kernel, as shown in Figures 8 and 9. The laminar flame speed is as low as 3.9 cm/s while the ESR is only 14 s^{-1}. Highly broken OH structures are found on both sides of the flame cone, due to a higher $Ka = 350$ in this case[3], also see the horizontal PLIF image in Figure 2. Among the three D cases, only D2 shows a large and continuous area below the ESR in the flame cone, consistent with the observation that D2 is the easiest case for flame stabilization, while the plate in D1 and D3 are approaching the closest ($L/D = 2$) and farthest ($L/D = 4$) horizontal distance between the nozzle and plate where the flame can be sustained. Heat loss to the wall may be of secondary importance since the mean flame brush position marked by $\bar{c} = 0.5$ remains away from the wall (12/16 mm in D2/D3), except for case D1 (only 3.5 mm to the mean flame brush position). Hence, apart from the mean strain rate K, two other possible mechanisms that push the flame to blow off as L/D is lowered are (1) heat loss to the wall; (2) the flame leading edge is forced too far upstream by the plate and to the left side of the burner center, see Figure 3(b) and Figure 8. As the plate is moved closer, eventually the flame front will meet the high velocity swirling

[3]A sample calculation of Ka can be found in the supplementary S2 in [12].

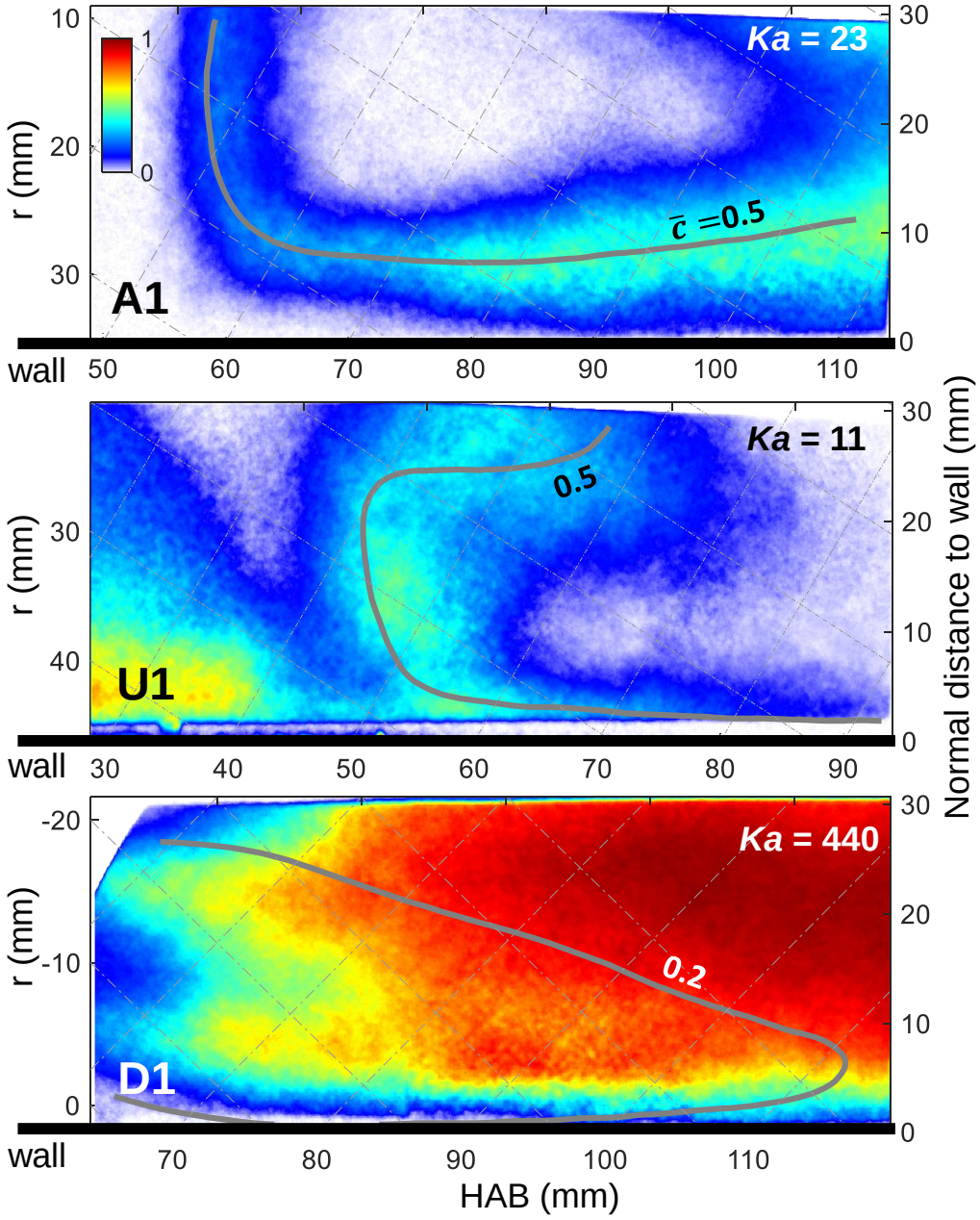

Figure 9: Probability map of CH_2O for A1, U1, and D1, calculated from the ensemble average of binarized CH_2O images.

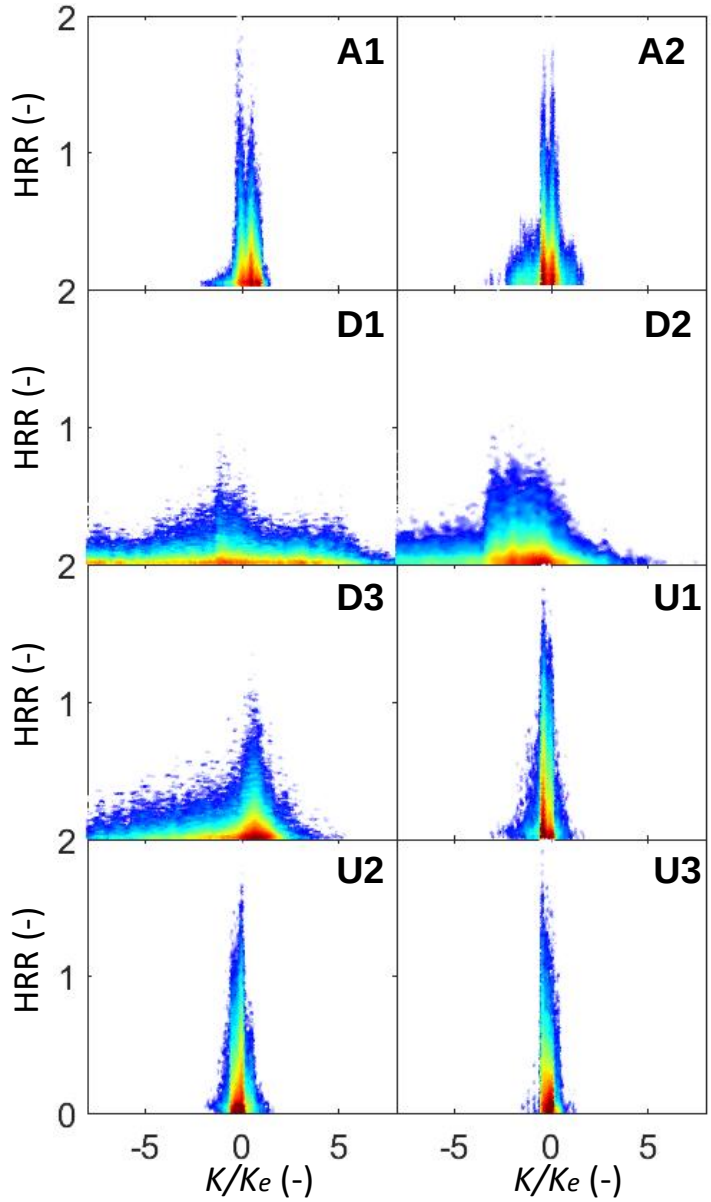

Figure 10: 2D joint PDFs between normalized HRR and mean strain rate. The mean strain rates are normalized by the ESR K_e of the corresponding case. Note that lateral comparison of the HRR values among A/U and D cases with different fuel compositions is not possible.

region as it climbs further downward along the plate, where the reactions can no longer survive due to both high shear and velocity magnitude. For large L/D, on the other hand, since the flame position is farther downstream, mixing with ambient air weakens the reactant mixture, such that the flame is too lean to be ignited.

We plot the correlation between normalized HRR and the mean strain rate (normalized by the ESR) in Figure 10. A clear difference can be observed between the A/U and D cases. Cases A1, D1, D3, and U1 are close to the blow off limit. The 100% CH_4 flames in A and U present a very narrow distribution of HRR, whose highest peak always resides in $|K|/K_e < 1$. Beyond this range, the reactions cannot survive for the methane flames. There are multiple peaks in A1 and A2, among which the two major ones are from the flame leading edge and the confined flame brush. In U1-U3, the scatter points are compacted due to a high ESR, only one sharp peak can be observed on the joint PDFs. In strong contrast to the 100% CH_4 cases, the HRR in D cases shows a much broader distribution in $|K|/K_e < 8$. This suggests the 70% H_2 flames can be stabilized well beyond the ESR obtained from 1D simulations. However, in these flames, the reaction zone is highly broken which results in incomplete combustion, accompanied by a very large formaldehyde cloud behind the reaction zone as shown in Figure 9.

6. Conclusion

The stabilization mechanisms of lean and ultra-lean swirling flames impinging on an inclined wall are investigated, by gradually adjusting the inclination angle, plate-nozzle distances, and bulk flow velocity, to the extreme positions or values where the flame can no longer be sustained. The flames are found to anchor at a low velocity region caused by the impingement. We also summarize the relation between the production of CH_2O and the mean strain rate. For 100% CH_4 cases at lean conditions ($\phi = 0.68$ and 0.78), flames mainly reside in areas where the mean strain rate is lower than the ESR. For high hydrogen fraction cases (70% H_2 in D cases), the flame front becomes highly broken and scattered in a wider area that is beyond the ESR. However, severe local quenching accompanied by a large cloud of CH_2O is identified in such conditions, suggesting stable but less efficient combustion.

Acknowledgments

The authors are thankful for the financial support from the NRC's Low-emission Aviation Program, the Office of Energy Research and Development (reference number NRC-19-123), Environment and Climate Change Canada, and the Natural Sciences and Engineering Research Council of Canada (grant numbers RGPIN-2019-04309, RGPAS-2019-00131). The first author further acknowledges the support from the NRC postdoctoral fellowship program. The flame calculations conducted by Mr. Mohammadreza Nozari (Polytechnique Montreal), and the technical support from Yin Yang and Mike Nguyen are also acknowledged.

References

[1] "National Academies of Sciences, Engineering, and Medicine", Advanced Technologies for Gas Turbines, The National Academies Press, Washington, DC, 2020. doi:10.17226/25630.

[2] S. Candel, Combustion dynamics and control: Progress and challenges, Proceedings of the Combustion Institute 29 (1) (2002) 1–28.

[3] J. Beita, M. Talibi, S. Sadasivuni, R. Balachandran, Thermoacoustic Instability Considerations for High Hydrogen Combustion in Lean Premixed Gas Turbine Combustors: A Review, Hydrogen 2 (1) (2021) 33–57.

[4] N. Peters, Turbulent Combustion, Cambridge University Press, 2000.

[5] B. Zhou, C. Brackmann, Z. Li, M. Aldén, X. S. Bai, Simultaneous multispecies and temperature visualization of premixed flames in the distributed reaction zone regime, Proceedings of the Combustion Institute 35 (2) (2015) 1409–1416.

[6] H. Wang, E. R. Hawkes, B. Savard, J. H. Chen, Direct numerical simulation of a high Ka CH4/air stratified premixed jet flame, Combustion and Flame 193 (2018) 229–245.

[7] F. Zentgraf, P. Johe, A. D. Cutler, R. S. Barlow, B. Böhm, A. Dreizler, Classification of flame prehistory and quenching topology in a side-wall quenching burner at low-intensity turbulence by correlating transport

effects with co2, co and temperature, Combustion and Flame 239 (2022) 111681.

[8] F. Zentgraf, P. Johe, M. Steinhausen, C. Hasse, M. Greifenstein, A. D. Cutler, R. S. Barlow, A. Dreizler, Detailed assessment of the thermochemistry in a side-wall quenching burner by simultaneous quantitative measurement of co2, co and temperature using laser diagnostics, Combustion and Flame 235 (2022) 111707.

[9] H. Kosaka, F. Zentgraf, A. Scholtissek, C. Hasse, A. Dreizler, Effect of Flame-Wall Interaction on Local Heat Release of Methane and DME Combustion in a Side-Wall Quenching Geometry, Flow, Turbulence and Combustion 104 (4) (2020) 1029–1046.

[10] Z. Wei, H. Zhen, C. Leung, C. Cheung, Z. Huang, Formations and emissions of CO/NO2/NOx in the laminar premixed biogas-hydrogen flame undergoing the flame-wall interaction: Effects of the variable CO2 proportion, Fuel 276 (May) (2020) 118096.

[11] E. C. Okafor, M. Tsukamoto, A. Hayakawa, K. A. Somarathne, T. Kudo, T. Tsujimura, H. Kobayashi, Influence of wall heat loss on the emission characteristics of premixed ammonia-air swirling flames interacting with the combustor wall, Proceedings of the Combustion Institute 38 (4) (2021) 5139–5146.

[12] L. Fan, B. Savard, S. Carlyle, M. Nozari, R. Naaman, B. Fond, P. Vena, Simultaneous stereo-PIV and OH×CH2O PLIF measurements in turbulent ultra lean CH4/H2 swirling wall-impinging flames, Proceedings of the Combustion Institute (nov 2022).

[13] Q. An, S. Kheirkhah, J. Bergthorson, S. Yun, J. Hwang, W. J. Lee, M. K. Kim, J. H. Cho, H. S. Kim, P. Vena, Flame stabilization mechanisms and shape transitions in a 3D printed, hydrogen enriched, methane/air low-swirl burner, International Journal of Hydrogen Energy 46 (27) (2021) 14764–14779.

[14] P. H. Paul, H. N. Najm, Planar laser-induced fluorescence imaging of flame heat release rate, Proceedings of the Combustion Institute 27 (1) (1998) 43–50.

[15] R. K. Cheng, S. A. Fable, D. Schmidt, L. Arellano, K. O. Smith, Development of a low swirl injector concept for gas turbines, 2000.
URL https://www.osti.gov/biblio/785290

[16] D. Kang, F. Culick, A. Ratner, Combustion dynamics of a low-swirl combustor, Combustion and Flame 151 (3) (2007) 412–425.

[17] S. Labuda, M. Karrer, J. Sotton, M. Bellenoue, Experimental study of single-wall flame quenching at high pressures, Combustion Science and Technology 183 (5) (2011) 409–426.

[18] G. P. Smith, D. M. Golden, M. Frenklach, N. W. Moriarty, B. Eiteneer, M. Goldenberg, C. T. Bowman, R. K. Hanson, S. Song, W. C. Gardiner, Jr., V. V. Lissianski, Z. Qin, http://combustion.berkeley.edu/gri-mech/.

[19] A. Aspden, M. Day, J. Bell, Towards the distributed burning regime in turbulent premixed flames, Journal of Fluid Mechanics 871 (2019) 1–21.

[20] A. J. Aspden, M. S. Day, J. B. Bell, Turbulence-flame interactions in lean premixed hydrogen: Transition to the distributed burning regime, Journal of Fluid Mechanics 680 (2011) 287–320.

[21] G. G. Szegö, B. B. Dally, G. J. Nathan, Operational characteristics of a parallel jet MILD combustion burner system, Combustion and Flame 156 (2) (2009) 429–438.

[22] T. Zirwes, T. Häber, F. Zhang, H. Kosaka, A. Dreizler, M. Steinhausen, C. Hasse, A. Stagni, D. Trimis, R. Suntz, H. Bockhorn, Numerical Study of Quenching Distances for Side-Wall Quenching Using Detailed Diffusion and Chemistry, Flow, Turbulence and Combustion 106 (2) (2021) 649–679.